ACS APPLIED MATERIALS & INTERFACES

Research Article

www.acsami.org

High-Performance Supercapacitor Electrode Materials from Cellulose-Derived Carbon Nanofibers

Jie Cai,[†,‡] Haitao Niu,[‡] Zhenyu Li,[‡] Yong Du,[‡] Pavel Cizek,[‡] Zongli Xie,[§] Hanguo Xiong,[†] and Tong Lin*[,‡]

[†]College of Food Science and Technology, Huazhong Agricultural University, Wuhan 430070, China

[‡]Institute for Frontier Materials, Deakin University, Geelong, Victoria 3216, Australia

[§]CSIRO Materials Science and Engineering, Clayton, Victoria 3169, Australia

Supporting Information

ABSTRACT: Nitrogen-functionalized carbon nanofibers (N-CNFs) were prepared by carbonizing polypyrrole (PPy)-coated cellulose NFs, which were obtained by electrospinning, deacetylation of electrospun cellulose acetate NFs, and PPy polymerization. Supercapacitor electrodes prepared from N-CNFs and a mixture of N-CNFs and $Ni(OH)_2$ showed specific capacitances of ~236 and ~1045 F g^{-1}, respectively. An asymmetric supercapacitor was further fabricated using N-CNFs/$Ni(OH)_2$ and N-CNFs as positive and negative electrodes. The supercapacitor device had a working voltage of 1.6 V in aqueous KOH solution (6.0 M) with an energy density as high as ~51 (W h) kg^{-1} and a maximum power density of ~117 kW kg^{-1}. The device had excellent cycle lifetime, which retained ~84% specific capacitance after 5000 cycles of cyclic voltammetry scans. N-CNFs derived from electrospun cellulose may be useful as an electrode material for development of high-performance supercapacitors and other energy storage devices.

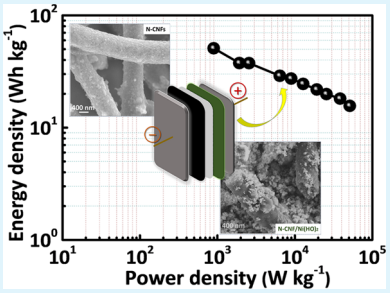

KEYWORDS: *nitrogen-functionalized carbon nanofiber, cellulose, nanofibers, electrospinning, supercapacitor*

INTRODUCTION

The supercapacitor represents a promising electrical energy storage device with a higher power density, a faster charge−discharge rate, and a longer cycle lifetime than conventional capacitors.[1−6] Especially, asymmetric supercapacitors such as those comprising a Faradaic electrode and a non-Faradaic (e.g., electric double-layer) electrode have drawn much attention because of the broad working voltage window, the improved energy density, and the high cycle stability.[7,8]

Carbon materials have been widely used for making supercapacitor electrodes because of the versatile forms (e.g., fibers, tubes, felts, and powders), the reasonable conductivity, and the excellent stability.[9−14] They contribute to over 80% of commercial supercapacitor products in the market.[15] To maximize electrode performance, nanostructured carbons with large surface area, highly porous structure, and oxidative groups (e.g., carboxylate, ketone, or hydroxyl) on the surface are often employed.[4,16−20] The surface modifications increase capacitance, accessibility to the electrolyte, and electrochemical activities. Recently, incorporating heteroatoms (e.g., nitrogen) into carbon lattice was also reported to enhance the pseudocapacitance, rate performance, and cycling stability of supercapacitors owing to the increased surface wettability, electrical conductivity, and electron-donor tendency of carbon materials.[21−27]

A wide range of nanocarbons (e.g., nanotube, graphene, nanofiber, and quantum dot) have been investigated for making supercapacitor electrodes.[28−31] Carbon nanofibers (NFs) from a polymer precursor prepared by electrospinning (electrostatic spinning) are distinct from the others in that they have various different fiber morphologies (e.g., hollow, porous, porous surfaced fiber, ribbon, spiral, and irregular cross-sectional fiber) and fibrous structures (e.g., aligned, randomly orientated, and interbonded). Electrospinning is advantageous in making polymer NFs with controlled fiber diameter, fiber alignment, and shape of the fibrous mat. It does not involve a tedious separation and dispersion process and use of harsh chemicals or catalysts.

Indeed, supercapacitor electrodes based on carbon NFs from electrospinning have shown high energy generation/storage performance.[32−34] The capacitance performance was also improved by adding additives (e.g., silver, nickel, or carbon nanotubes) to the carbon NFs,[35−37] applying conducting polymers (e.g., polypyrrole)[38] or transition metal oxides (e.g., RuO_2)[39] on the fiber surface. Niu et al.[9] from our group reported using interbonded carbon NFs to reduce internal resistance and improve charge transfer within a carbon electrode, hence increasing the capacitance.

However, most of the carbon NFs from electrospinning are prepared using polyacrylonitrile, polybenzimidazol, or pitch as the carbon source,[34,40,41] which release toxic substances during carbonization. Carbon NFs made from a largely available

Received: April 30, 2015
Accepted: June 18, 2015
Published: June 18, 2015

DOI: 10.1021/acsami.5b03757
ACS Appl. Mater. Interfaces 2015, 7, 14946−14953

precursor source with minimal pollutant emission during preparation is highly desired.[42] To this end, cellulose is an excellent candidate because it comes from an inexhaustible natural resource with high sustainability.[43,44] The annual production volume of cellulose is estimated to reach 1.5 trillion tons.[45] Cellulose consists of just the elements carbon, hydrogen, and oxygen, and its carbonization releases mainly carbon dioxide and water.[46] Cellulose has no apparent melting point, and it maintains its physical morphology after being carbonized. However, cellulose has poor electrospinning ability.[43,47,48] Although cellulose derivatives, for example, cellulose acetate (CA) and ethyl cellulose, have much improved electrospinning ability, they typically melt before carbonization, ruining the fibrous morphology.

In this study, we develop an effective method to prepare nitrogen-functionalized carbon nanofibers (N-CNFs) using a multistep method: (1) electrospinning CA into uniform NFs, (2) immersing as-spun NFs into an alkaline solution to convert CA into cellulose meanwhile maintaining the fibrous morphology, (3) applying polypyrrole (PPy) onto cellulose NFs using an in situ polymerization method, and (4) direct carbonization of the PPy-coated NFs into carbon NFs. Electrodes prepared by the N-CNFs show high specific capacitance and excellent cycling stability. Using N-CNFs and $Ni(OH)_2$ containing a small portion of N-CNFs as the negative and positive electrodes, respectively, we further prepared an asymmetric supercapacitor and proved that the supercapacitor device had a working voltage of 1.6 V in 6.0 M aqueous KOH solution with an energy density as high as ~51 (W h) kg^{-1} and a maximum power density of ~117 kW kg^{-1}. The device can retain 84% of the specific capacitance after 5000 cycles of cyclic voltammetry (CV) scans.

RESULTS AND DISCUSSION

Figure 1 schematically illustrates the procedure to prepare carbon NFs and the supercapacitor device. Uniform CA NFs

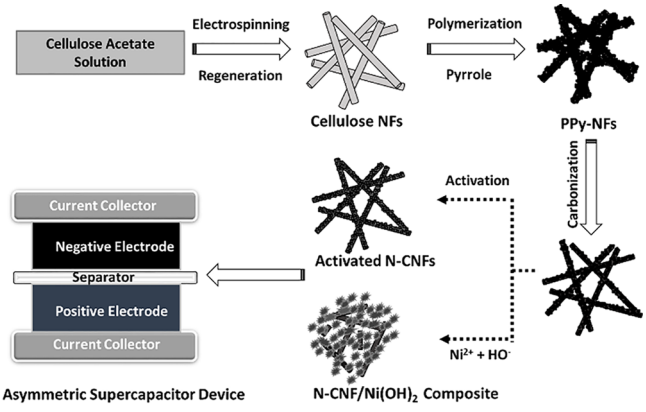

Figure 1. Schematic illustration of the procedure to prepare NF electrode materials and the supercapacitor device.

(diameter = 694 ± 193 nm) were prepared by electrospinning (see the morphology in the Supporting Information). The CA NFs were then immersed in a NaOH–ethanol solution to convert the CA into cellulose. After immersion, the fibers retained their morphology (see the Supporting Information) with a diameter of 666 ± 206 nm. Fourier transform IR (FTIR), differential scanning calorimetry (DSC), and X-ray diffraction (XRD) measurements confirmed that the CA NFs after NaOH treatment were fully deacetylated, forming cellulose NFs (see detail results in the Supporting Information).

PPy was applied onto the cellulose NFs through solution polymerization of pyrrole in the presence of cellulose NFs. After polymerization, the fibers became rough on the surface (see the Supporting Information). The chemical component and solid characteristic of the PPy-coated nanofibers (PPy-NFs) were characterized by FTIR spectroscopy, X-ray photoelectron spectroscopy (XPS), XRD, and thermogravimetric analysis (TGA), verifying the success in synthesis of PPy on the fiber surface (see detail results in the Supporting Information).

Carbon NFs were prepared by directly carbonizing PPy-NFs at a high temperature. Figure 2b shows the scanning electron

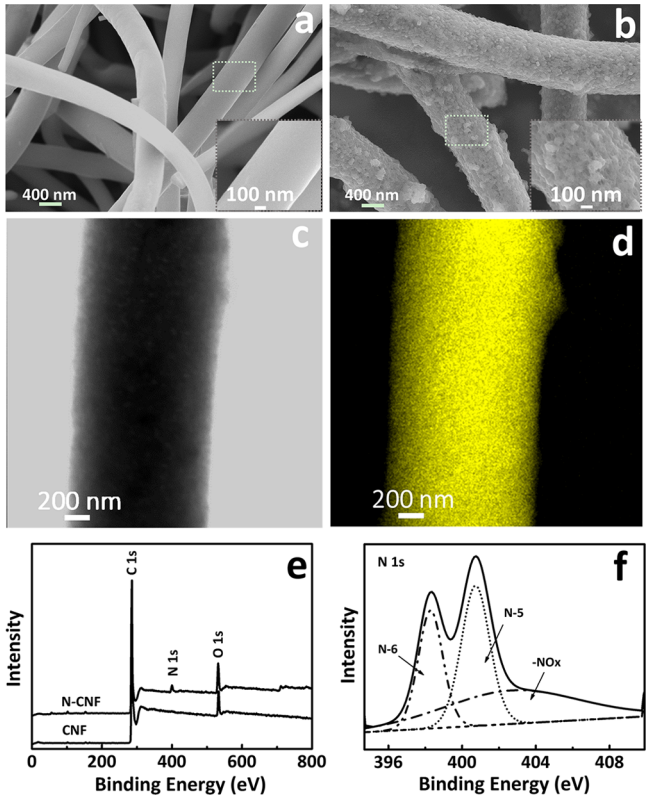

Figure 2. (a, b) SEM images of CNFs and N-CNFs, respectively; (c) TEM image of N-CNFs; (d) corresponding TEM-EDS image of N; (e) XPS survey spectra; (f) high-resolution XPS N 1s spectrum of N-CNFs.

microscopy (SEM) image of the carbonized PPy-NFs, which have a rough surface. The carbonized NFs reduced the diameter to 634 ± 130 nm. For comparison, cellulose NFs without PPy were also subjected to the same carbonization process. However, the carbonized cellulose NFs had a smooth surface with a diameter of 536 ± 106 nm (Figure 2a). The rough surface on the carbonized PPy-NFs came from PPy particles.

Transmission electron microscopy energy dispersive X-ray spectroscopy (TEM-EDS) mapping and XPS were used to characterize the elementary distribution of the carbonized NFs (Figure 2c, d). As shown in Figure 2d, N distributes uniformly throughout the carbonized PPy-NF surface. The XPS survey spectrum indicated that N existed in the carbonized PPy-NFs, with a N/C atomic ratio of 1:23.5 (Figure 2f). For the CNFs,

DOI: 10.1021/acsami.5b03757
ACS Appl. Mater. Interfaces 2015, 7, 14946–14953

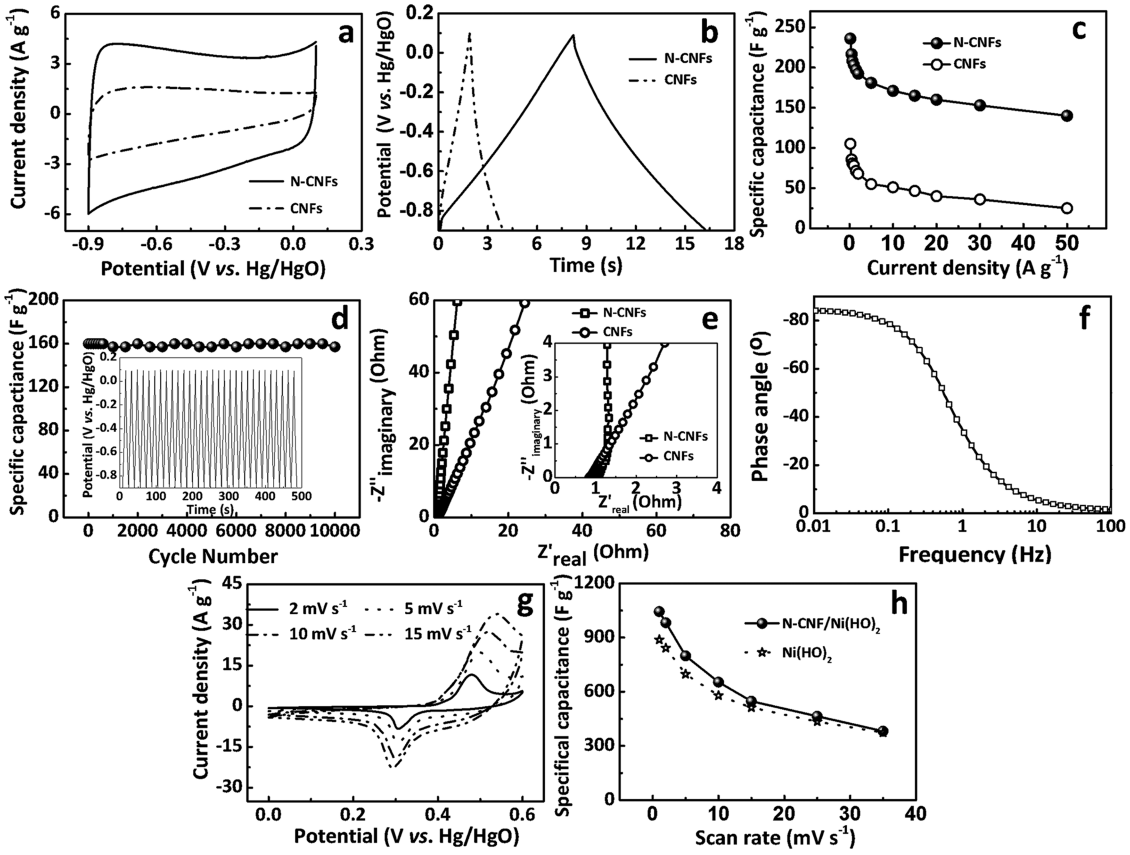

Figure 3. (a) Typical CV curves of CNFs and N-CNF electrodes at a scan rate of 20 mV s^{-1}; (b) typical GCD curves of CNFs and N-CNF electrodes at a current density of 20 A g^{-1}; (c) specific capacitance of CNFs and N-CNF electrodes at different current densities; (d) cycling ability of the N-CNF electrode at a current density of 20 A g^{-1} (the inset shows a GCD curve of the first 30 cycles); (e) Nyquist plots of CNFs and N-CNF electrodes (inset: magnified 0−4 Ω region); (f) plot of the impedance of phase angle versus frequency for the N-CNF electrode; (g) CV curves of the N-CNF/$Ni(OH)_2$ electrode at various scan rates; (h) specific capacitance of $Ni(OH)_2$ and N-CNF/$Ni(OH)_2$ electrodes as a function of the scan rates based on the CV curves.

however, no N was found on the surface. This result indicates that N-CNFs are formed when PPy is applied onto the cellulose NFs before carbonization. Figure 2f shows the high-resolution XPS N 1s spectrum of the N-CNFs. The two main peaks with binding energies at ∼398.3 and ∼400.7 eV correspond to pyridinic and pyrrolic/pyridone N, respectively. The curve-fitting of the spectrum revealed that a broad peak at about 403.1 eV also existed, which is assigned to −NOx. These N-containing groups are expected to function like active sites to strengthen the capacitive properties.

The surface area and pore size of the carbon nanofibers were measured (see the Supporting Information). The N-CNFs showed lower pore volume ascribing to the destruction of pore walls and blocking of the pore due to N doping.[49] A similar result was also reported in the literature.[26,50] In spite of this, N-CNFs still showed a reasonably high surface area (∼281.8 m^2 g^{-1}), and the pores in the NFs had a mean size of ∼3.47 nm. These microspores were formed due the treatment in CO_2 atmosphere at the final carbonization stage. The treatment in CO_2 is also referred to as "activation". Such a microporous structure could facilitate the transport and diffusion of electrolyte ions during charge and discharge, especially at a high current density, and it reduces the internal resistance (R_{int}), leading to high supercapacitor performance.[26,50,51]

Figure 3 shows the electrochemical property of the carbon NFs measured using a three-electrode system in 6.0 M aqueous KOH solution. N-CNFs had a nearly rectangular CV curve, indicating excellent capacitive behavior (Figure 3a). The CV curve still kept the "quasi-rectangular shapes" even at a scan rate of 200 mV s^{-1} (see the Supporting Information), indicating the good reversibility and low equivalent series resistance (ESR). In comparison, CNFs showed a small rectangular CV curve. The area surrounded by the CV curve for N-CNFs was significantly larger than that of CNFs both at low and high scan rates (see the Supporting Information), suggesting that the N-CNFs have higher capacitance than the CNFs. This can be explained by the combined electric double-layer capacitance (EDLC) and pseudocapacitance from the N-functionalized carbon.[52]

The galvanostatic charge/discharge (GCD) performance was measured at a voltage window that was the same as the CV test. Figure 3b shows the GCD curve of CNFs and N-CNFs at the current density of 20 A g^{-1}, and GCD curves at different current densities are shown in the Supporting Information. With increasing the current density, the discharge time increased. However, the N-CNF electrode had an evidently longer discharge time than the CNF electrode, suggesting that N-CNFs offer a much larger capacitance, which agrees well with the CV testing results. In addition, a small drop of the R_{int} drop was observed in the GCD curves, indicating a small overall resistance. The N-CNF electrode had nearly linear and symmetrical GCD curves, indicating the excellent EDLC characteristic and electrochemical reversibility, as well as the rapid $I-V$ response.

DOI: 10.1021/acsami.5b03757
ACS Appl. Mater. Interfaces 2015, 7, 14946−14953

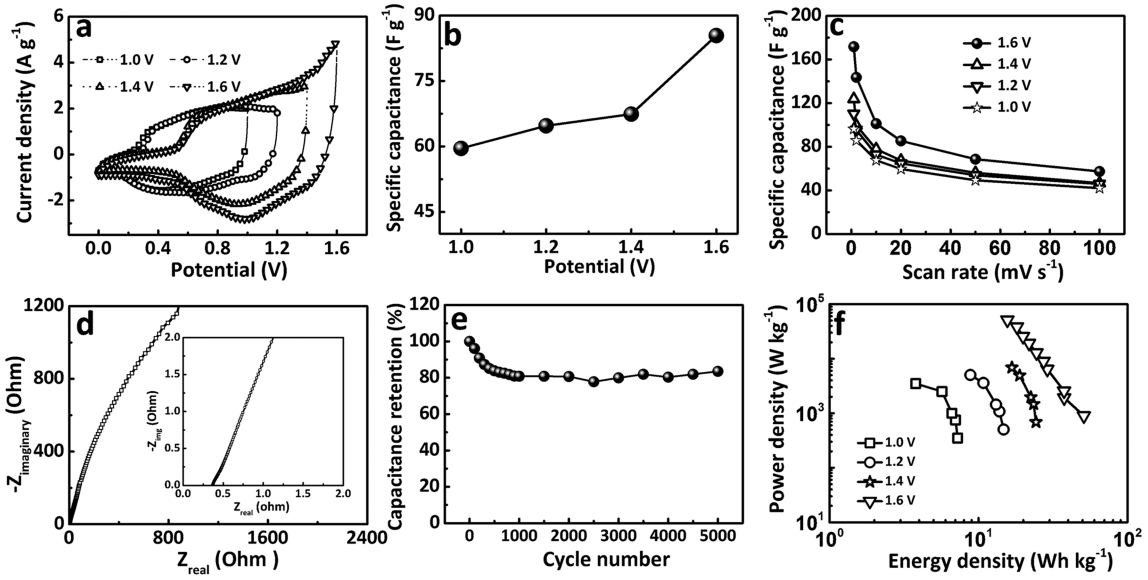

Figure 4. (a) CV curves of the device at different operation voltages (scan rate, 20 mV s^{-1}); (b) effect of operation voltage range on the specific capacitance (scan rate, 20 mV s^{-1}); (c) specific capacitance at different scan rates; (d) Nyquist plots (inset: magnified 0−2 Ω region); (e) cycle performance within a voltage of 1.6 V (scan rate, 100 mV s^{-1}); (f) Ragone plot related to energy and power densities operated at different operation voltages.

The specific capacitance (C_s) of a single electrode was calculated based on the galvanostatic discharge curve according to eq 1:[10]

$$C_s = \frac{I \times \Delta t}{m \times \Delta V} \quad (1)$$

where I is the discharge current (A), ΔV (V) is the potential change within the discharge time Δt (s), and m is the mass of the electrode (g). Figure 3c shows the effect of the charge−discharge current density on the specific capacitance. The N-CNF electrode had a specific capacitance of ∼236 F g^{-1} at 0.2 A g^{-1}, which is substantially higher than that of the CNF electrode (∼105 F g^{-1}). The specific capacitance of the N-CNF electrode maintained as high as ∼171 F g^{-1} at 10 A g^{-1}, ∼84.1% retention at 1 A g^{-1} (∼203.4 F g^{-1}), indicating a good capacitance retention capability and nonkinetic limited performance.[10,53] The high rate capability makes this material suitable for high power supercapacitor applications. This capacitance value is higher than most of the N-functionalized carbon materials reported in the literature (see Table S2 in the Supporting Information). The N-CNF electrode also exhibited an excellent cycling stability with less than 2% capacitance loss after 10 000 cycles of charge−discharge at a high current density of 20 A g^{-1} (Figure 3d).

Electrochemical impedance spectroscopy (EIS) was used to understand the ion-transfer behavior and electrical resistance of the electrode materials (Figure 3e). In the high-frequency range, the solution resistance and the charge-transfer resistance can be obtained from the intercept and the semicircle intercept at the $Ź_{real}$, respectively. It was obvious that the solution resistance and the charge-transfer resistance for N-CNFs were very small (<1.1 Ω), suggesting low ESR in the electrode materials. In the low-frequency region, the linear part called Warburg resistance presents the diffusion behavior of electrolyte ions within the electrodes. Such behavior is caused by the interruptions during the semi-infinite diffusion of ions into the porous structure. The steep slope of Warburg curves indicates fast formation of an electric double-layer. The ion-penetration process was characterized by the projected length at the $Ź_{real}$. The N-CNF electrode had a more vertical curve than the CNF electrode, suggesting that the N-functionalized material has a shorter ion diffusion and a better capacitor performance.

Figure 3f shows the impedance phase angles of the N-CNF electrode at different frequencies. The characteristic frequency f_0 for a phase angle of 45° marked the point at which the resistive and capacitive impedances had equal magnitudes.[54,55] On the basis of f_0, A time constant ($t_0 = 1/f_0$) is based on f_0 and indicates how fast the electrode materials can be charged and discharged reversibly. The small time constant (t_0 = 1.5s) for the N-CNF electrode suggests a comparable charged−discharged speed to microporous- or mesoporous-activated carbon electrodes.

We further proved that the N-CNFs can be used as a negative electrode to prepare an asymmetric supercapacitor. To prepare an asymmetric supercapacitor, $Ni(OH)_2$ was chosen as the positive electrode material. $Ni(OH)_2$ nanoparticles were synthesized by a solid-state reaction in the presence of a small portion of N-CNFs (nonactivated). Here, N-CNFs were added to increase the conductivity of $Ni(OH)_2$. $Ni(OH)_2$ nanoparticles distributed evenly throughout the fibrous matrix. In comparison, $Ni(OH)_2$ nanoparticles without N-CNFs were also prepared, which showed particle cluster morphology (see the Supporting Information).

The XRD measurement indicated that $Ni(OH)_2$ was in a hexagonal phase regardless of the presence of N-CNFs, which is in good agreement with the reported β-type $Ni(OH)_2$ phase (see the Supporting Information).[56] The N-CNFs/$Ni(OH)_2$ composite showed weaker XRD diffraction peaks than pure $Ni(OH)_2$, attributive to the dispersion of the carbon materials in the resulting composite.[57] The chemical composition of the N-CNFs/$Ni(OH)_2$ composite was also proved by the XPS results (see the result in the Supporting Information).

Figure 3g shows the CV curves of the N-CNFs/$Ni(OH)_2$ electrode at different scan rates. All the CV curves contained two peaks, corresponding to an anodic peak at ∼0.48 V and a

DOI: 10.1021/acsami.5b03757
ACS Appl. Mater. Interfaces 2015, 7, 14946−14953

cathodic peak at ~0.30 V. These two redox peaks are ascribed to the faradic reaction of $Ni(OH)_2$:[55]

$$Ni(OH)_2 + OH^- \leftrightarrow NiOOH + H_2O + e^-$$

The CV curves showed a similar profile when the scan rate was in the range 2−15 mV s^{-1}. With increasing the scan rate, the potential of both the anodic and the cathodic peaks shifted toward more positive and negative directions, due to the increased internal diffusion resistance of electrode.[57,58]

Voltammetric currents are known to be directly proportional to the scan rate and thereby display capacitive behavior.[59] The N-CNFs/$Ni(OH)_2$ electrode exhibited improved electrochemical properties, making it promising for a supercapacitor (Figure 3h). The N-CNFs/$Ni(OH)_2$ composite electrode can reach a specific capacitance as high as ~1045 F g^{-1} at 1 mV s^{-1}. The enhanced performance can be ascribed to the positive synergistic effect of carbon NFs and $Ni(OH)_2$. $Ni(OH)_2$ nanoparticles on carbon NFs allow good access to the electrolyte, and the carbon substrate endows the electrode with high electrical conductivity effectively facilitating the redox reaction.[22,57] With increasing of the scan rate, the specific capacitance declined accordingly; however, the trend was much slower than that of the $Ni(OH)_2$ electrode. This is because the diffusion of protons within the electrode is limited at high charge−discharge rates and parts of the electrode surface are inaccessible, which results in incomplete sustenance for the redox transition in the inner active sites.[60]

An asymmetric supercapacitor device was fabricated using N-CNFs/$Ni(OH)_2$ and N-CNFs as positive and negative electrodes. The mass loading ratio of the positive and the negative electrode materials was calculated according to eq 2:[61]

$$\frac{m_+}{m_-} = \frac{C_- \times V_-}{C_+ \times V_+} \quad (2)$$

where C (F g^{-1}), V (V), and m (g) are the capacitance, the charging−discharging voltage range, and the mass of the electrode, respectively. The supercapacitor using 6.0 M aqueous KOH solution as the electrolyte was tested in a two-electrode configuration. Figure 4a shows the CV curves with different voltage windows. Stable CV curves resulted even if the potential window was as large as 1.6 V. The redox peaks in the CV curves indicated the pseudocapacitive behavior of the device because of the faradaic reaction of $Ni(OH)_2$. With increasing the potential window, the faradaic reactions become more intensive.

Figure 4b shows the specific capacitance calculated based on the CV curves. The capacitance value increased from ~59.6 to ~85.4 F g^{-1} when the potential range increased from 1.0 to 1.6 V. The GCD curves of the device still remained nearly symmetric even at a potential of 1.6 V (see the Supporting Information), indicating the excellent capacitive characteristics with a rapid $I-V$ response and small ESR. Therefore, the voltage window of 1.6 V was chosen for further study of the device electrochemical properties.

Figure 4c shows the effect of scan rate on specific capacitance. With increasing of the scan rate, the specific capacitance decreased gradually. This can be explained by the decrease in the electrochemical utilization of electroactive materials at a high scan rate.[62] The capacitor device operated at the window of 1.6 V and the scan rate of 1 mV s^{-1} had a high specific capacitance of ~172 F g^{-1}, which was approximately 1.4, 1.6, and 1.8 times higher than that at a voltage window of 1.4, 1.2, and 1.0 V (same scan rate), respectively.

The GCD curve at different current densities exhibited almost equilateral triangle shapes at a potential of 1.6 V (see the Supporting Information), suggesting good reversibility and desirable fast charge−discharge property.[50] R_{int} drop ($R_{int,drop}$) was obtained based on the GCD curves, and the effect of the discharge current density on the $R_{int,drop}$ was shown in the Supporting Information (Figure S11c). The $R_{int,drop}$ and the current were in a linear relationship, according to eq 3:[63]

$$R_{int,drop} = a + bI \quad (3)$$

where a is the difference between the applied potential of 1.6 V and the charged potential of the capacitor and b is double the value of the internal resistance R_s (Ω). The small R_s of the device would assist in delivering high discharge power in practical applications.[26] The capacitor device showed a phase angle close to 90° for frequencies up to 100 Hz (see Figure S11d in the Supporting Information), a characteristic capacitor behavior.[64]

Figure 4d shows Nyquist plots of the capacitor device. The charge-transfer resistance was calculated based on the Nyquist curve. The maximum power density (P_{max}) can be calculated by eq 4:[63]

$$P_{max} = \frac{V_0^2}{4 \times M \times R_s} = \frac{(1.6 - a)^2}{2 \times M \times b} \quad (4)$$

Here, V_0 is the practical work potential of the device (V). The maximum power density reached ~117 kW kg^{-1}, which is comparable with most of the other reported nickel-based or nitrogen-containing aqueous electrolyte supercapacitors.[58,65−67]

The long-term cycling stability of the device was measured by repeating the CV scan at a scan rate of 100 mV s^{-1} for 5000 cycles. The capacitance as a function of the scan cycle is shown in Figure 4e. The device retained ~81% of the initial value after the initial 1000 scan cycles and a slight increase in the capacitance to ~84% of the initial capacitance after 5000 cycles. The pulverization and loss of electrical contact between the active material and the carbon could be the cause to the initial decrease in the capacitance, whereas the capacitance increase at the later stage could come from the improvement in the electrode surface wettability.[57]

Figure 4f shows Ragone plots of asymmetric supercapacitor devices. The energy density decreased when the specific power density increased. The maximum energy density for our asymmetric supercapacitor operating at the 1.6 V voltage window was ~51 (W h) kg^{-1} at a power density of ~0.9 kW kg^{-1}. These data are higher than those of the supercapacitors made of other electrospun materials reported.[68−70] It is also comparable to some nickel-based asymmetric supercapacitors with an aqueous solution electrolyte and significantly higher than the symmetrical supercapacitor (see Table S3 in the Supporting Information).

The excellent performance of the asymmetric supercapacitor device can be explained by two main reasons: (1) N-CNFs with high surface area, appropriate porosity, and good electric conductivity provide enormous active sites for electrochemical reaction, short ion-diffusion path, and fast charge-transfer speed during charge−discharge; and (2) nanosized $Ni(OH)_2$ enhances the capacitance and rate performance.

DOI: 10.1021/acsami.5b03757
ACS Appl. Mater. Interfaces 2015, 7, 14946−14953

CONCLUSIONS

We have fabricated N-CNFs using PPy-coated cellulose electrospun NFs as the precursor. The N-CNFs show high specific capacitance and excellent cycling stability when they are used as an electrode material. Using the N-CNFs as the negative electrode material and $Ni(OH)_2$/N-CNFs as the positive electrode material, we have further prepared an asymmetric supercapacitor and proved that the supercapacitor device has high specific capacitance, high energy density, and good cycling stability with an operating voltage of 1.6 V in KOH aqueous electrolyte, which exceeds the supercapacitor devices made of other electrospun NF electrode materials and some other asymmetric supercapacitors. N-CNFs derived from electrospun cellulose may serve as a promising electrode material for high-performance supercapacitor and other energy storage devices.

EXPERIMENTAL SECTION

Material. Pyrrole (Sigma–Aldrich, 98%), nickel acetate tetrahydrate (Sigma–Aldrich), sodium hydroxide (Merck KGaA), potassium hydroxide (Chem-Supply), ferric chloride (Ajax Chemicals), oxalic acid (Acros, 98%), and hydrochloric acid (RCI Labscan, 32%) were used as received.

Preparation of Cellulose NFs. CA NFs were prepared using a purpose-built electrospinning setup. The as-spun NFs were then immersed in 0.1 M NaOH–ethanol solution at room temperature for 24 h to convert the CA within the NFs into cellulose. After washing with deionized water, the NaOH-treated NFs were dried under vacuum to get cellulose NFs.

Coating of PPy on Cellulose NFs. Cellulose NFs (0.3 g) were immersed in an aqueous HCl solution (1.0 M) containing pyrrole (1.8 g), followed by stirring for 2 h. Ferric chloride solution was added dropwise to the NF-containing solution, and the mixture was then stirred for an another 18 h in an ice–water bath. The PPy-coated NFs were separated by filtration, washed with distilled water and ethanol, and dried under vacuum at 60 °C. The molar ratio of pyrrole/$FeCl_3$ in the coating solution was 1:1.

Preparation of N-CNF Electrode Material. PPy-NFs were carbonized in a tubular furnace at 850 °C for 2 h in N_2 atmosphere. To activate the carbon fibers, the products were heated in CO_2 at 850 °C for 2 h at the final stage of the carbonization process. For comparison, cellulose NFs without PPy were also subjected to the same procedure to get CNFs.

Preparation of N-CNFs/$Ni(OH)_2$ Electrode Material. The N-CNFs/$Ni(OH)_2$ composite was prepared using a two-step solid-state reaction route from the literature[55] with some modification. In the first step, nickel acetate and oxalic acid (mole ratio = 1:1) were mixed and ground in an agate mortar for 0.5 h, followed by filtering with water and ethanol. In the second step, the dried precursor (0.2 g) and N-CNFs (0.022 g) (without activated during carbonization) were ground together with a mortar. After 0.5 h, KOH (0.123 g) was added into the mixture under continuous grinding at ambient temperature for additional 1.0 h. The final product was rinsed with water and then dried at 80 °C to obtain the N-CNFs/$Ni(OH)_2$ composite. The mass fraction of $Ni(OH)_2$ in the composite was 82%. For comparison, the same procedure was also employed to prepare pure $Ni(OH)_2$ without N-CNFs.

Electrochemical Characterization. All electrochemical measurements were carried out on a CHI 760D electrochemical workstation. The electrodes were prepared by mixing active material, carbon black, and poly(vinylidene fluoride) in *N*-methylpyrrolidone at a mass ratio of 80:15:5 to obtain a slurry. The slurry was then pressed onto a nickel foam current collector (1 cm × 1 cm) and dried at 80 °C overnight. The electrochemical test of the individual electrode was carried out on a three-electrode system using platinum foil as the counter electrode, a Hg/HgO electrode as the reference electrode, and 6.0 M aqueous KOH solution as the electrolyte. The asymmetric supercapacitor device was fabricated by separating two electrodes with filter paper. The supercapacitor was tested in a two-electrode system. All the electrochemical tests were carried out at room temperature. The specific capacitance (C_m) of the asymmetric supercapacitor was calculated based on the galvanostatic discharge curve using the following equation:[50]

$$C_m = \frac{I \times \Delta t}{M \times \Delta V} \tag{5}$$

where M is the total mass of the active materials on the two electrodes of the capacitor (g). The key parameters of the supercapacitor, power density (P) (W g^{-1}) and energy density (E) (J g^{-1}), were calculated using eqs 6 and 7:[10,16,71]

$$E = \frac{1}{2} \times C_m \times (\Delta V)^2 \tag{6}$$

$$P_{av} = \frac{E}{\Delta t} \tag{7}$$

Other Characterizations. The microstructure was observed under a scanning electron microscope (Supra 55VP) and a transmission electron microscope (JEOL 2100F). The crystallographic structure was analyzed on a powder X-ray diffractometer (X'pert Pro MRD XL) equipped with Cu Kα radiation (λ = 0.15406 nm). The surface chemical composition was characterized using an X-ray photoelectron spectrometer (Kratos AXIS Ultra DLD) equipped with a 165 mm hemispherical electron energy analyzer. The incident radiation was monochromatic Al X-rays (1486.6 eV) at 150 W (15 kV, 10 mA). FTIR spectroscopy was measured on a Bruker VERTEX 70 spectrometer with ATR mode. DSC was conducted on a TA Q200 equipment at a 10 °C/min heating rate. TGA was performed on a TA Q50 in N_2 atmosphere with a heating rate of 10 °C/min and a temperature range from 30 to 800 °C. The Brunauer–Emmett–Teller (BET) surface area was measured by the nitrogen adsorption method with a Quantachrome Autosorb-1 instrument. The pore size distributions was determined by the density functional theory method.

ASSOCIATED CONTENT

Supporting Information

SEM images, photos, FTIR spectra, DSC curves, XRD patterns, XPS spectra, TGA thermograms, BET nitrogen absorption curves, electrochemical results, and comparison of a supercapacitor. The Supporting Information is available free of charge on the ACS Publications website at DOI: 10.1021/acsami.5b03757.

AUTHOR INFORMATION

Corresponding Author

*E-mail: tong.lin@deakin.edu.au.

Notes

The authors declare no competing financial interest.

ACKNOWLEDGMENTS

Financial support from the National Natural Science Foundation of China (no. 31471699), the National Science & Technology Support Program (no. 2012BAD54G01), the Huazhong Agricultural University Scientific & Technological Self-innovation Foundation (no. 2012SC21), the Fundamental Research Funds for the Central Universities (no. 2011PY152), and the scholarship from Chinese Scholarship Council awarded to the first author to visit Deakin University is acknowledged.

REFERENCES

(1) Giri, S.; Ghosh, D.; Das, C. K. Growth of Vertically Aligned Tunable Polyaniline on Graphene/ZrO_2 Nanocomposites for Super-

DOI: 10.1021/acsami.5b03757
ACS Appl. Mater. Interfaces 2015, 7, 14946–14953

capacitor Energy-Storage Application. *Adv. Funct. Mater.* **2014**, *24*, 1312−1324.
(2) Wang, H. L.; Liang, Y. Y.; Mirfakhrai, T.; Chen, Z.; Casalongue, H. S.; Dai, H. J. Advanced Asymmetrical Supercapacitors Based on Graphene Hybrid Materials. *Nano Res.* **2011**, *4*, 729−736.
(3) Shen, J. L.; Yang, C. Y.; Li, X. W.; Wang, G. C. High-Performance Asymmetric Supercapacitor Based on Nanoarchitectured Polyaniline/Graphene/Carbon Nanotube and Activated Graphene Electrodes. *ACS Appl. Mater. Interfaces* **2013**, *5*, 8467−8476.
(4) Zhang, L. L.; Zhao, X. S. Carbon-Based Materials as Supercapacitor Electrodes. *Chem. Soc. Rev.* **2009**, *38*, 2520−2531.
(5) Yu, Z.; Chen, L.; Song, L.; Zhu, Y.; Ji, H.; Yu, S. Free-Standing Boron and Oxygen Co-Doped Carbon Nanofiber Films for Large Volumetric Capacitance and High Rate Capability Supercapacitors. *Nano Energy* **2015**, *15*, 235−243.
(6) Chen, L. F.; Yu, Z. Y.; Wang, J. J.; Li, Q. X.; Tan, Z. Q.; Zhu, Y. W.; Yu, S. H. Metal-like Fluorine-Doped β-FeOOH Nanorods Grown on Carbon Cloth for Scalable High-Performance Supercapacitors. *Nano Energy* **2015**, *11*, 119−128.
(7) Wang, F. X.; Xiao, S. Y.; Hou, Y. Y.; Hu, C. L.; Liu, L. L.; Wu, Y. P. Electrode Materials for Aqueous Asymmetric Supercapacitors. *RSC Adv.* **2013**, *3*, 13059−13084.
(8) Choi, B. G.; Yang, M.; Hong, W. H.; Choi, J. W.; Huh, Y. S. 3D Macroporous Graphene Frameworks for Supercapacitors with High Energy and Power Densities. *ACS Nano* **2012**, *6*, 4020−4028.
(9) Niu, H. T.; Zhang, J.; Xie, Z. L.; Wang, X. G.; Lin, T. Preparation, Structure and Supercapacitance of Bonded Carbon Nanofiber Electrode Materials. *Carbon* **2011**, *49*, 2380−2388.
(10) Chen, L. F.; Zhang, X. D.; Liang, H. W.; Kong, M. G.; Guan, Q. F.; Chen, P.; Wu, Z. Y.; Yu, S. H. Synthesis of Nitrogen-Doped Porous Carbon Nanofibers as an Efficient Electrode Material for Supercapacitors. *ACS Nano* **2012**, *6*, 7092−7102.
(11) Dai, L. M.; Chang, D. W.; Baek, J. B.; Lu, W. Carbon Nanomaterials for Advanced Energy Conversion and Storage. *Small* **2012**, *8*, 1130−1166.
(12) Ghosh, A.; Lee, Y. H. Carbon-Based Electrochemical Capacitors. *ChemSusChem* **2012**, *5*, 480−499.
(13) Pandolfo, A.; Hollenkamp, A. Carbon Properties and Their Role in Supercapacitors. *J. Power Sources* **2006**, *157*, 11−27.
(14) Frackowiak, E. Carbon Materials for Supercapacitor Application. *Phys. Chem. Chem. Phys.* **2007**, *9*, 1774−1785.
(15) Hao, L.; Li, X. L.; Zhi, L. J. Carbonaceous Electrode Materials for Supercapacitors. *Adv. Mater.* **2013**, *25*, 3899−3904.
(16) Chen, T.; Dai, L. M. Carbon Nanomaterials for High-Performance Supercapacitors. *Mater. Today* **2013**, *16*, 272−280.
(17) Aricò, A. S.; Bruce, P.; Scrosati, B.; Tarascon, J. M.; Van Schalkwijk, W. Nanostructured Materials for Advanced Energy Conversion and Storage Devices. *Nat. Mater.* **2005**, *4*, 366−377.
(18) Frackowiak, E.; Beguin, F. Carbon Materials for the Electrochemical Storage of Energy in Capacitors. *Carbon* **2001**, *39*, 937−950.
(19) Han, J.; Zhang, L. L.; Lee, S.; Oh, J.; Lee, K. S.; Potts, J. R.; Ji, J.; Zhao, X.; Ruoff, R. S.; Park, S. Generation of B-Doped Graphene Nanoplatelets Using a Solution Process and Their Supercapacitor Applications. *ACS Nano* **2012**, *7*, 19−26.
(20) Lin, Z. Y.; Liu, Y.; Yao, Y. G.; Hildreth, O. J.; Li, Z.; Moon, K.; Agar, J. C.; Wong, C. P. Superior Capacitance of Functionalized Graphene. *J. Phys. Chem. C* **2011**, *115*, 14041−14047.
(21) Zhao, L.; Hu, Y. S.; Li, H.; Wang, Z. X.; Chen, L. Q. Porous $Li_4Ti_5O_{12}$ Coated with N-Doped Carbon from Ionic Liquids for Li-Ion Batteries. *Adv. Mater.* **2011**, *23*, 1385−1388.
(22) Long, C.; Qi, D.; Wei, T.; Yan, J.; Jiang, L.; Fan, Z. Nitrogen-Doped Carbon Networks for High Energy Density Supercapacitors Derived from Polyaniline Coated Bacterial Cellulose. *Adv. Funct. Mater.* **2014**, *24*, 3953−3961.
(23) Pan, H. L.; Zhao, L.; Hu, Y. S.; Li, H.; Chen, L. Q. Improved Li-Storage Performance of $Li_4Ti_5O_{12}$ Coated with C—N Compounds Derived from Pyrolysis of Urea through a Low-Temperature Approach. *ChemSusChem* **2012**, *5*, 526−529.
(24) Xu, B.; Zheng, D. F.; Jia, M. Q.; Cao, G. P.; Yang, Y. S. Nitrogen-Doped Porous Carbon Simply Prepared by Pyrolyzing a Nitrogen-Containing Organic Salt for Supercapacitors. *Electrochim. Acta* **2013**, *98*, 176−182.
(25) Han, J.; Xu, G.; Ding, B.; Pan, J.; Dou, H.; MacFarlane, D. R. Porous Nitrogen-Doped Hollow Carbon Spheres Derived from Polyaniline for High Performance Supercapacitors. *J. Mater. Chem. A* **2014**, *2*, 5352−5357.
(26) Chen, L. F.; Huang, Z. H.; Liang, H. W.; Gao, H. L.; Yu, S. H. Three-Dimensional Heteroatom-Doped Carbon Nanofiber Networks Derived from Bacterial Cellulose for Supercapacitors. *Adv. Funct. Mater.* **2014**, *24*, 5104−5111.
(27) Guo, B.; Sun, X. G.; Veith, G. M.; Bi, Z.; Mahurin, S. M.; Liao, C.; Bridges, C.; Paranthaman, M. P.; Dai, S. Nitrogen-Enriched Carbons from Alkali Salts with High Coulombic Efficiency for Energy Storage Applications. *Adv. Energy Mater.* **2013**, *3*, 708−712.
(28) Liu, W. W.; Feng, Y. Q.; Yan, X. B.; Chen, J. T.; Xue, Q. J. Superior Micro-Supercapacitors Based on Graphene Quantum Dots. *Adv. Funct. Mater.* **2013**, *23*, 4111−4122.
(29) Su, D. S.; Schlögl, R. Nanostructured Carbon and Carbon Nanocomposites for Electrochemical Energy Storage Applications. *ChemSusChem* **2010**, *3*, 136−168.
(30) Simon, P.; Gogotsi, Y. Capacitive Energy Storage in Nanostructured Carbon−Electrolyte Systems. *Acc. Chem. Res.* **2012**, *46*, 1094−1103.
(31) Bose, S.; Kuila, T.; Mishra, A. K.; Rajasekar, R.; Kim, N. H.; Lee, J. H. Carbon-Based Nanostructured Materials and Their Composites as Supercapacitor Electrodes. *J. Mater. Chem.* **2012**, *22*, 767−784.
(32) Cavaliere, S.; Subianto, S.; Savych, I.; Jones, D. J.; Roziere, J. Electrospinning: Designed Architectures for Energy Conversion and Storage Devices. *Energy Environ. Sci.* **2011**, *4*, 4761−4785.
(33) Dong, Z. X.; Kennedy, S. J.; Wu, Y. Q. Electrospinning Materials for Energy-Related Applications and Devices. *J. Power Sources* **2011**, *196*, 4886−4904.
(34) Thavasi, V.; Singh, G.; Ramakrishna, S. Electrospun Nanofibers in Energy and Environmental Applications. *Energy Environ. Sci.* **2008**, *1*, 205−221.
(35) Li, J.; Liu, E.-h.; Li, W.; Meng, X.-y.; Tan, S.-t. Nickel/Carbon Nanofibers Composite Eectrodes as Supercapacitors Prepared by Electrospinning. *J. Alloys Compd.* **2009**, *478*, 371−374.
(36) Guo, Q.; Zhou, X.; Li, X.; Chen, S.; Seema, A.; Greiner, A.; Hou, H. Supercapacitors Based on Hybrid Carbon Nanofibers Containing Multiwalled Carbon Nanotubes. *J. Mater. Chem.* **2009**, *19*, 2810−2816.
(37) Park, S. J.; Im, S. H. Electrochemical Behaviors of PAN/Ag-Based Carbon Nanofibers by Electrospinning. *Bull. Korean Chem. Soc.* **2008**, *29*, 777−781.
(38) Ju, Y. W.; Choi, G. R.; Jung, H. R.; Lee, W. J. Electrochemical Properties of Electrospun PAN/MWCNT Carbon Nanofibers Electrodes Coated with Polypyrrole. *Electrochim. Acta* **2008**, *53*, 5796−5803.
(39) Ahn, Y. R.; Park, C. R.; Jo, S. M.; Kim, D. Y. Enhanced Charge-Discharge Characteristics of RuO_2 Supercapacitors on Heat-Treated TiO_2 Nanorods. *Appl. Phys. Lett.* **2007**, *90*, 122106−122106−3.
(40) Inagaki, M.; Yang, Y.; Kang, F. Y. Carbon Nanofibers Prepared via Electrospinning. *Adv. Mater.* **2012**, *24*, 2547−2566.
(41) Gu, S. Y.; Wu, Q. L.; Ren, J. Preparation and Surface Structures of Carbon Nanofibers Produced from Electrospun PAN Precursors. *New Carbon Mater.* **2008**, *23*, 171−176.
(42) Hu, B.; Wang, K.; Wu, L. H.; Yu, S. H.; Antonietti, M.; Titirici, M. M. Engineering Carbon Materials from the Hydrothermal Carbonization Process of Biomass. *Adv. Mater.* **2010**, *22*, 813−828.
(43) Deng, L.; Young, R. J.; Kinloch, I. A.; Zhu, Y.; Eichhorn, S. J. Carbon Nanofibres Produced from Electrospun Cellulose Nanofibres. *Carbon* **2013**, *58*, 66−75.
(44) Dumanli, A. G.; Windle, A. H. Carbon Fibres from Cellulosic Precursors: A Review. *J. Mater. Sci.* **2012**, *47*, 4236−4250.
(45) Klemm, D.; Heublein, B.; Fink, H. P.; Bohn, A. Cellulose: Fascinating Biopolymer and Sustainable Raw Material. *Angew. Chem., Int. Ed.* **2005**, *44*, 3358−3393.

DOI: 10.1021/acsami.5b03757
ACS Appl. Mater. Interfaces 2015, 7, 14946−14953

(46) Grainger, D.; Hägg, M.-B. Evaluation of Cellulose-Derived Carbon Molecular Sieve Membranes for Hydrogen Separation from Light Hydrocarbons. *J. Membr. Sci.* **2007**, *306*, 307−317.
(47) Lu, P.; Hsieh, Y. L. Multiwalled Carbon Nanotube (MWCNT) Reinforced Cellulose Fibers by Electrospinning. *ACS Appl. Mater. Interfaces* **2010**, *2*, 2413−2420.
(48) Kuzmenko, V.; Naboka, O.; Gatenholm, P.; Enoksson, P. Ammonium Chloride Promoted Synthesis of Carbon Nanofibers from Electrospun Cellulose Acetate. *Carbon* **2014**, *67*, 694−703.
(49) Sun, L.; Wang, L.; Tian, C.; Tan, T.; Xie, Y.; Shi, K.; Li, M.; Fu, H. Nitrogen-Doped Graphene with High Nitrogen Level via a One-Step Hydrothermal Reaction of Graphene Oxide with Urea for Superior Capacitive Energy Storage. *RSC Adv.* **2012**, *2*, 4498−4506.
(50) Chen, L. F.; Huang, Z. H.; Liang, H. W.; Guan, Q. F.; Yu, S. H. Bacterial-Cellulose-Derived Carbon Nanofiber@MnO_2 and Nitrogen-Doped Carbon Nanofiber Electrode Materials: An Asymmetric Supercapacitor with High Energy and Power Density. *Adv. Mater.* **2013**, *25*, 4746−4752.
(51) Wang, D. W.; Li, F.; Liu, M.; Lu, G. Q.; Cheng, H. M. 3D Aperiodic Hierarchical Porous Graphitic Carbon Material for High-Rate Electrochemical Capacitive Energy Storage. *Angew. Chem., Int. Ed.* **2008**, *47*, 373−376.
(52) Kim, W.; Kang, M. Y.; Joo, J. B.; Kim, N. D.; Song, I. K.; Kim, P.; Yoon, J. R.; Yi, J. Preparation of Ordered Mesoporous Carbon Nanopipes with Controlled Nitrogen Species for Application in Electrical Double-Layer Capacitors. *J. Power Sources* **2010**, *195*, 2125−2129.
(53) Yang, L.; Cheng, S.; Ding, Y.; Zhu, X. B.; Wang, Z. L.; Liu, M. L. Hierarchical Network Architectures of Carbon Fiber Paper Supported Cobalt Oxide Nanonet for High-Capacity Pseudocapacitors. *Nano Lett.* **2012**, *12*, 321−325.
(54) Ma, C.; Song, Y.; Shi, J.; Zhang, D.; Zhai, X.; Zhong, M.; Guo, Q.; Liu, L. Preparation and One-Step Activation of Microporous Carbon Nanofibers for Use as Supercapacitor Electrodes. *Carbon* **2013**, *51*, 290−300.
(55) Sheng, K.; Sun, Y.; Li, C.; Yuan, W.; Shi, G. Ultrahigh-Rate Supercapacitors Based on Eletrochemically Reduced Graphene Oxide for ac Line-Filtering. *Sci. Rep.* **2012**, *2*, 1−5.
(56) Liu, X. H.; Yu, L. Synthesis of Nanosized Nickel Hydroxide by Solid-State Reaction at Room Temperature. *Mater. Lett.* **2004**, *58*, 1327−1330.
(57) Yan, J.; Fan, Z.; Sun, W.; Ning, G.; Wei, T.; Zhang, Q.; Zhang, R.; Zhi, L.; Wei, F. Advanced Asymmetric Supercapacitors Based on $Ni(OH)_2$/Graphene and Porous Graphene Electrodes with High Energy Density. *Adv. Funct. Mater.* **2012**, *22*, 2632−2641.
(58) Ji, J.; Zhang, L. L.; Ji, H.; Li, Y.; Zhao, X.; Bai, X.; Fan, X.; Zhang, F.; Ruoff, R. S. Nanoporous $Ni(OH)_2$ Thin Film on 3D Ultrathin-Graphite Foam for Asymmetric Supercapacitor. *ACS Nano* **2013**, *7*, 6237−6243.
(59) Patil, U. M.; Gurav, K. V.; Fulari, V. J.; Lokhande, C. D.; Joo, O. S. Characterization of Honeycomb-like "β-$Ni(OH)_2$" Thin Films Synthesized by Chemical Bath Deposition Method and Their Supercapacitor Application. *J. Power Sources* **2009**, *188*, 338−342.
(60) Jiang, H.; Zhao, T.; Li, C. Z.; Ma, J. Hierarchical Self-Assembly of Ultrathin Nickel Hydroxide Nanoflakes for High-Performance Supercapacitors. *J. Mater. Chem.* **2011**, *21*, 3818−3823.
(61) Khomenko, V.; Raymundo-Pinero, E.; Beguin, F. Optimisation of an Asymmetric Manganese Oxide/Activated Carbon Capacitor Working at 2 V in Aqueous Medium. *J. Power Sources* **2006**, *153*, 183−190.
(62) Lao, Z. J.; Konstantinov, K.; Tournaire, Y.; Ng, S. H.; Wang, G. X.; Liu, H. K. Synthesis of Vanadium Pentoxide Powders with Enhanced Surface-Area for Electrochemical Capacitors. *J. Power Sources* **2006**, *162*, 1451−1454.
(63) Izadi-Najafabadi, A.; Yasuda, S.; Kobashi, K.; Yamada, T.; Futaba, D. N.; Hatori, H.; Yumura, M.; Iijima, S.; Hata, K. Extracting the Full Potential of Single-Walled Carbon Nanotubes as Durable Supercapacitor Electrodes Operable at 4 V with High Power and Energy Density. *Adv. Mater.* **2010**, *22*, E235−E241.
(64) Du, C. S.; Pan, N. Supercapacitors Using Carbon Nanotubes Films by Electrophoretic Deposition. *J. Power Sources* **2006**, *160*, 1487−1494.
(65) Qiu, Y.; Zhang, X.; Yang, S. High Performance Supercapacitors Based on Highly Conductive Nitrogen-Doped Graphene Sheets. *Phys. Chem. Chem. Phys.* **2011**, *13*, 12554−12558.
(66) Tan, Y.; Xu, C.; Chen, G.; Liu, Z.; Ma, M.; Xie, Q.; Zheng, N.; Yao, S. Synthesis of Ultrathin Nitrogen-Doped Graphitic Carbon Nanocages as Advanced Electrode Materials for Supercapacitor. *ACS Appl. Mater. Interfaces* **2013**, *5*, 2241−2248.
(67) Wang, X. F.; Ruan, D. B.; You, Z. Application of Spherical $Ni(OH)_2$/CNTs Composite Electrode in FP Asymmetric Supercapacitor. *Trans. Nonferrous Met. Soc. China* **2006**, *16*, 1129−1134.
(68) Wang, J. G.; Yang, Y.; Huang, Z. H.; Kang, F. Y. A High-Pperformance Asymmetric Supercapacitor Based on Carbon and Carbon-MnO_2 Nanofiber Electrodes. *Carbon* **2013**, *61*, 190−199.
(69) Mak, W. F.; Wee, G.; Aravindan, V.; Gupta, N.; Mhaisalkar, S. G.; Madhavi, S. High-Energy Density Asymmetric Supercapacitor Based on Electrospun Vanadium Pentoxide and Polyaniline Nanofibers in Aqueous Electrolyte. *J. Electrochem. Soc.* **2012**, *159*, A1481−A1488.
(70) Vidyadharan, B.; Abd Aziz, R.; Misnon, I. I.; Kumar, G. M. A.; Ismail, J.; Yusoff, M. M.; Jose, R. High Energy and Power Density Asymmetric Supercapacitors Using Electrospun Cobalt Oxide Nanowire Anode. *J. Power Sources* **2014**, *270*, 526−535.
(71) Zhu, Y.; Murali, S.; Stoller, M. D.; Ganesh, K.; Cai, W.; Ferreira, P. J.; Pirkle, A.; Wallace, R. M.; Cychosz, K. A.; Thommes, M. Carbon-Based Supercapacitors Produced by Activation of Graphene. *Science* **2011**, *332*, 1537−1541.

DOI: 10.1021/acsami.5b03757
ACS Appl. Mater. Interfaces 2015, 7, 14946−14953